Proceedings of the Eighteenth International Conference on
Civil, Structural and Environmental Engineering Computing
Edited by: P. Iványi, J. Kruis and B.H.V. Topping
Civil-Comp Conferences, Volume 10, Paper 3.7
Civil-Comp Press, Edinburgh, United Kingdom, 2025
ISSN: 2753-3239, doi: 10.4203/ccc.10.3.7

Topology Optimization of Thermo-Elastic Cyclic-Symmetric Structures Considering Mean Stress Constraints

Z. Li[1], C. Zhang[1,2], C. Ma[2], T. Gao[1], L. Meng[1] and W. Zhang[1]

[1]State IJR Center of Aerospace Design and Additive Manufacturing, Northwestern Polytechnical University, Xi'an, China
[2]AECC Sichuan Gas Turbine Establishment, Chengdu, China

Abstract

The thermo-elastic cyclic-symmetric structures such as turbine disks in aerospace engines operate under complex loading conditions, requiring precise burst speed analysis to balance safety and lightweight design. This study introduces a novel topology optimization framework that integrates mean circumferential/radial stress constraints derived from burst speed requirements, addressing the limitations of conventional retrospective validation methods. By transforming rotational speed constraints into equivalent stress limits, the approach proactively optimizes material distribution while considering multi-physics coupling. Key techniques include the coordinate transformation for stress analysis, adjoint-based sensitivity analysis, and advanced relaxation strategy of stress-based constraints. A numerical case of an annular structure validates the method: compared to unconstrained optimization, the proposed framework reduces the mean stress by 8.87% while maintaining structural compliance within a 30% volume fraction constraint. Optimized designs exhibit branching structures that effectively redistribute stress concentrations. This work bridges theoretical burst speed analysis with proactive topology optimization, offering a systematic solution to enhance cyclic-symmetric structures safety margins and material efficiency.

Keywords: topology optimization, mean stress constraints, burst speed, cyclic-symmetric structures, relaxation strategy, sensitivity analysis.

1 Introduction

The cyclic-symmetric structures such as turbine disks are critical structural components in aerospace engines, subject to complex loading conditions including centrifugal forces from high-speed rotation, thermal stresses due to non-uniform temperature distributions, gas pressure, and assembly stresses at connection interfaces [1]. Analyzing their burst speed is fundamental for strength design, with international standards mandating a burst speed reserve coefficient exceeding 1.22 for turbine disks [2]. Given the catastrophic consequences of non-inclusive disk rupture [3, 4] and the weight constraints imposed by engine thrust-to-weight ratios, optimizing disk designs requires a delicate balance between burst speed analysis and lightweight objectives. Overly conservative predictions increase structural mass, while underpredictions risk premature failure.

Originating from Robinson's 1944 Mean Stress Method [5], the field has evolved through empirical and computational refinements. NASA's material utilization coefficients [6] and GE's notch strength calibration improved practical applicability, while modern studies like Xie et al. [7] introduced probabilistic models for burst speed prediction, accounting for material uncertainty and structural reliability. Kasljevic [8] correlated numerical simulations with experimental burst tests, bridging theoretical analysis and real-world validation. Computational advancements, such as Zhu et al.'s [9] failure assessment diagram for burst speed evaluation, have enhanced accuracy by integrating global stability criteria and finite element discretization.

The conventional mean stress method for burst speed prediction faces inherent limitations as a reverse-engineering approach that requires iterative validation of pre-existing configurations. This retrospective validation process inevitably prolongs development cycles and escalates costs, prompting the exploration of topology optimization (TO) as a proactive design strategy. TO fundamentally integrates structural performance constraints during conceptual design phases while offering substantial design freedom, particularly when combined with additive manufacturing advancements [10-12]. Defined as the systematic determination of optimal material distribution within specified design domains under predefined objectives and constraints, TO has evolved significantly since Bendsøe and Kikuchi's pioneering homogenization-based methodology [13]. Three principal branches have emerged: a) Density-based methods employing Solid Isotropic Material with Penalization (SIMP) [14-16] or Rational Approximation of Material Properties (RAMP) [17, 18]; b) Evolutionary Structural Optimization (ESO) [19, 20]; and c) Level-Set Methods (LSM) [21, 22].

Notwithstanding these advancements, significant challenges persist in optimizing designs under operational loads such as thermal gradients and centrifugal forces. The inherent coupling between structural configuration and load distribution necessitates concurrent consideration of both elements during optimization. Current research predominantly focuses on two areas: stiffness maximization [23-27] and stress-based optimization [28-30], with some studies combining both approaches [31-34]. However, a critical research gap remains unaddressed: the systematic treatment of

mean stress constraints specifically governing disk burst rotational speeds. This lacuna in current literature highlights the necessity for novel methodologies that can effectively reconcile structural topology optimization with burst speed-driven mean stress requirements.

This study introduces a novel topology optimization framework of thermo-elastic cyclic-symmetric structures with mean circumferential/radial stress constraints derived from burst speed requirements. By transforming rotational speed constraints into equivalent stress limits, the method enables proactive design optimization, balancing structural compliance with safety margins. The proposed approach integrates coordinate transformation techniques, adjoint-based sensitivity analysis, and relaxtion strategy of stress-based constraints, providing a systematic solution for cyclic-symmetric structures design.

2 Mean circumferential/radial stress constraint

The mean stress method is defined as a failure criterion where circumferential or radial rupture occurs when the mean circumferential stress in the meridional cross-section or the mean radial stress at any radius reaches the corresponding ultimate strength of the material. Empirical formulas based on numerical solutions of the mean stress method have been developed in engineering for predicting burst speeds. When conducting stress analysis using the finite element method, simplified calculation methods for circumferential/radial stresses in disks can be employed [35]. In such cases, the formula for calculating disk burst speed in cylindrical coordinates is expressed as follows:

$$\omega_{\text{burst}} = \omega_{\max}\sqrt{\frac{\zeta\bar{\sigma}_b}{\bar{\sigma}_{\theta/r}}} \tag{1}$$

where ω_{burst} and $\omega_{\max}$ represent the burst speed and allowable maximum speed of the disk respectively, such that the burst speed reserve coefficient η can be expressed as the ratio $\omega_{\text{burst}}/\omega_{\max}$. ζ denotes the material utilization coefficient of the disk. $\bar{\sigma}_b$ corresponds to the tensile strength of the material when separation or rupture occurs in the meridional or cylindrical cross-section of the turbine disk at the mean operating temperature. $\bar{\sigma}_{\theta/r}$ represents the mean circumferential stress or mean radial stress of the turbine disk.

Based on the expression method for burst speed using the mean stress method, the constraint expression for the burst speed of the turbine disk can be formulated as follows:

$$\begin{aligned}\omega_{\text{burst},\theta} &= \omega_{\max}\sqrt{\frac{\zeta\bar{\sigma}_{\text{b}\theta}}{\bar{\sigma}_\theta}} \geq \omega_\theta \\ \omega_{\text{burst},r} &= \omega_{\max}\sqrt{\frac{\zeta\bar{\sigma}_{\text{b}}}{\bar{\sigma}_r}} \geq \omega_r\end{aligned} \tag{2}$$

where ω_θ and ω_r denote the specified lower constraint limits for circumferential and radial burst speeds respectively.

As derived from the preceding analysis, the burst speed constraint fundamentally constitutes a mean circumferential/radial stress constraint, yielding the transformed expression:

$$\begin{aligned} \bar{\sigma}_\theta &\le \zeta \bar{\sigma}_{\mathrm{b}\theta} \left(\frac{\omega_{\mathrm{burst},\theta}}{\omega_\theta} \right)^2 = \zeta \bar{\sigma}_{\mathrm{b}\theta} \eta_\theta^2 \\ \bar{\sigma}_r &\le \zeta \bar{\sigma}_{\mathrm{b}} \left(\frac{\omega_{\mathrm{burst},r}}{\omega_r} \right)^2 = \zeta \bar{\sigma}_{\mathrm{b}} \eta_r^2 \end{aligned} \tag{3}$$

where η_θ and η_r respectively stand for the circumferential burst safety factor and the radial burst speed safety factor of the turbine disk. Every parameter on the right-hand side of the constraint inequality can be set through experimental methods or empirical data. As a result, the upper constraint limit of the mean circumferential stress or mean radial stress of the disk can be precisely calculated. This idea offers a systematic way to transform the rotational speed-related design constraints into equivalent stress-based constraints.

Here, the mean circumferential and radial stresses previously described are formulated within the cylindrical coordinate system. To facilitate sensitivity analysis and subsequent topology optimization algorithm development, a coordinate transformation method can be employed to approximate the stress matrix in cylindrical coordinates using the Cartesian stress matrix. In the Cartesian coordinate system, assuming fixed hexahedral element dimensions, the mean circumferential and radial stresses of the disk based on finite element method can be approximated by multiplying the differential area of the mean stress integration cross-section by a uniform thickness. The expressions are as follows:

$$\begin{aligned} \bar{\sigma}_\theta &= \frac{1}{V_{\mathrm{sum}}} \sum_{e=1}^{n} \left(\sigma_{e,\theta} V_e \right) \\ \bar{\sigma}_r &= \frac{1}{V_{\mathrm{sum}}} \sum_{e=1}^{n} \left(\sigma_{e,r} V_e \right) \end{aligned} \tag{4}$$

where $\sigma_{e,\theta}$ denotes the circumferential stress of element e, $\sigma_{e,r}$ represents the radial stress of element e, V_e designates the volume of the e-th element, and V_{sum} denotes the total volume.

In general, for the Cartesian and cylindrical coordinate systems sharing the same origin and z-axis, the transformation relationship between Cartesian coordinates (x, y, z) and cylindrical coordinates (r, θ, z) can be mathematically expressed as:

$$\begin{aligned} x &= r \cos\theta \\ y &= r \sin\theta \end{aligned} \tag{5}$$

Moreover, based on the relationship between the cylindrical coordinate system and the Cartesian coordinate system, the directional transformation matrix $\boldsymbol{\beta}$ can be formed as:

$$\boldsymbol{\beta} = \begin{bmatrix} \cos\theta & \sin\theta & 0 \\ -\sin\theta & \cos\theta & 0 \\ 0 & 0 & 1 \end{bmatrix} \tag{6}$$

Let $\boldsymbol{\sigma}_{\text{Cartesian}}$ and $\boldsymbol{\sigma}_{\text{cylindrical}}$ denote the stress tensor matrices in the Cartesian and cylindrical coordinate systems, respectively, which can be expressed as:

$$\boldsymbol{\sigma}_{\text{Cartesian}} = \begin{bmatrix} \sigma_x & \tau_{xy} & \tau_{xz} \\ \tau_{yx} & \sigma_y & \tau_{yz} \\ \tau_{zx} & \tau_{zy} & \sigma_z \end{bmatrix} \quad \boldsymbol{\sigma}_{\text{cylindrical}} = \begin{bmatrix} \sigma_r & \tau_{r\theta} & \tau_{rz} \\ \tau_{\theta r} & \sigma_\theta & \tau_{\theta z} \\ \tau_{zr} & \tau_{z\theta} & \sigma_z \end{bmatrix} \tag{7}$$

From Equation (6), the element stress tensor matrix in the cylindrical coordinate system can be expressed by the stress matrix in the Cartesian coordinate system and the directional transformation matrix $\boldsymbol{\beta}$ as follows:

$$\boldsymbol{\sigma}_{\text{cylindrical}} = \boldsymbol{\beta}^{\text{T}} \boldsymbol{\sigma}_{\text{Cartesian}} \boldsymbol{\beta} \tag{8}$$

Therefore, the detailed expressions of $\sigma_{e,\theta}$ and $\sigma_{e,r}$ in Equation (4) can be further derived as:

$$\begin{aligned} \sigma_{e,\theta} &= \sigma_{e,x} \sin^2\theta_e + \sigma_{e,y} \cos^2\theta_e - \tau_{e,xy} \sin 2\theta_e \\ \sigma_{e,r} &= \sigma_{e,x} \sin^2\theta_e + \sigma_{e,y} \cos^2\theta_e + \tau_{e,xy} \sin 2\theta_e \end{aligned} \tag{9}$$

Herein, θ_e represents the azimuthal angle of element e, which can be approximately calculated from the coordinates of the element centroid (X_e, Y_e, Z_e) using the arctangent function.

Considering the element stress vector $\boldsymbol{\sigma}_e = \left[\sigma_{e,x}, \sigma_{e,y}, \sigma_{e,z}, \tau_{e,xy}, \tau_{e,yz}, \tau_{e,xz}\right]^{\text{T}}$ in the finite element method, according to Equation (9), Equation (4) can be rewritten in the form of the sum of vector dot-products:

$$\begin{aligned} \bar{\sigma}_\theta &= \frac{1}{V_{\text{sum}}} \sum_{e=1}^{n} \left(\sigma_{e,\theta} V_e\right) = \frac{1}{V_{\text{sum}}} \sum_{e=1}^{n} \left(\boldsymbol{S}_{e,\theta} \boldsymbol{\sigma}_e V_e\right) \\ \bar{\sigma}_r &= \frac{1}{V_{\text{sum}}} \sum_{e=1}^{n} \left(\sigma_{e,r} V_e\right) = \frac{1}{V_{\text{sum}}} \sum_{e=1}^{n} \left(\boldsymbol{S}_{e,r} \boldsymbol{\sigma}_e V_e\right) \end{aligned} \tag{10}$$

where the coordinate transformation vectors $\mathbf{S}_{e,\theta}$ and $\mathbf{S}_{e,r}$ are explicitly defined through the following expressions:

$$\begin{aligned}\mathbf{S}_{e,\theta} &= \begin{bmatrix} \sin^2\theta_e & \cos^2\theta_e & 0 & -\sin 2\theta_e & 0 & 0 \end{bmatrix} \\ \mathbf{S}_{e,r} &= \begin{bmatrix} \cos^2\theta_e & \sin^2\theta_e & 0 & \sin 2\theta_e & 0 & 0 \end{bmatrix}\end{aligned} \tag{11}$$

3 Topology optimization

3.1 Optimization formulation

Building upon the previously described research framework, this study develops a topological optimization formulation considering mean stress constraints for thermo-elastic cyclic-symmetric structures. The optimization problem is formulated to minimize the global structural compliance, subject to constraints on mean circumferential stress, mean radial stress, and volume fraction ratio. The detailed mathematical expressions are explicitly formulated as follows:

$$\begin{aligned}
&\text{find:} && \mathbf{x} = \{x_i\},\ i = 1, 2, 3, \mathrm{L}\ , n_{\mathrm{d}} \\
&\text{minimize:} && C = \frac{1}{2}\mathbf{U}^{\mathrm{T}}\mathbf{K}\mathbf{U} \\
&\text{subject to:} && \bar{x}_i = \Psi_i(\mathbf{x}),\ i = 1, 2, 3, \mathrm{L}\ , n_{\mathrm{d}} \\
& && \mathbf{K}\mathbf{U} = \mathbf{F}^{\mathrm{m}} + \mathbf{F}^{\mathrm{th}} + \mathbf{F}^{\mathrm{ct}} \\
& && \bar{\sigma}_\theta = \frac{1}{V_{\mathrm{sum}}}\sum_{e=1}^{n_{\mathrm{d}}}\left(\mathbf{S}_{e,\theta}\boldsymbol{\sigma}_e V_e\right) \le \zeta\bar{\sigma}_{\mathrm{b}\theta}\eta_\theta^2 \\
& && \bar{\sigma}_r = \frac{1}{V_{\mathrm{sum}}}\sum_{e=1}^{n_{\mathrm{d}}}\left(\mathbf{S}_{e,r}\boldsymbol{\sigma}_e V_e\right) \le \zeta\bar{\sigma}_{\mathrm{b}}\eta_r^2 \\
& && \sum_{i=1}^{n_{\mathrm{d}}}\bar{x}_i V_i \le f_V V \\
& && 0 < x_{\min} \le x_i \le 1
\end{aligned} \tag{12}$$

Herein, **x** denotes the design variable vector, where each component x_i represents an independent design variable defined on the i-th designable element, and n_{d} is the total number of designable elements in the structure. C signifies the global structural compliance, with **U** and **K** representing the global displacement matrix and global stiffness matrix, respectively. $\bar{x}_i$ denotes the filtered density obtained via the filtering function $\psi_i(\mathbf{x})$, which will be detailed in subsequent sections. $\bar{\sigma}_\theta$ and $\bar{\sigma}_r$ are the mean circumferential and radial stresses defined previously, for which appropriate upper constraint limits can be specified. V_i represents the volume of element i, V is the total volume of the structural design domain, and f_V is the prescribed volume fraction upper limit. $x_{\min}$ is the specified lower bound of the design variable, set to $x_{\min} = 10^{-3}$ to prevent singularity of the stiffness matrix in finite element analysis. $\mathbf{F}^{\mathrm{m}}$, $\mathbf{F}^{\mathrm{th}}$, and $\mathbf{F}^{\mathrm{ct}}$ correspond to mechanical, thermal, and centrifugal loads, where the latter two are design-variable-dependent. Their expressions are given by:

$$\mathbf{F}^{\mathrm{th}} = \sum_{e=1}^{N_e} \mathbf{F}_e^{\mathrm{th}} = \sum_{e=1}^{N_e} \int_{V_e} \mathbf{B}_e^{\mathrm{T}} \mathbf{D}_e \alpha_e \mathbf{I} \Delta T_e dV \tag{13}$$

and

$$\mathbf{F}^{\mathrm{ct}} = \sum_{e=1}^{N_e} \mathbf{F}_e^{\mathrm{th}} = \sum_{e=1}^{N_e} \omega^2 \mathbf{M}_e \mathbf{R}_e \tag{14}$$

where the subscript e denotes quantities associated with a finite element. The strain-displacement matrix $\mathbf{B}_e$ and elasticity matrix $\mathbf{D}_e$ characterize the element's mechanical behavior, while α_e represents the material's linear thermal expansion coefficient, and ΔT_e is the scalar temperature change within the element. Volumetric thermal expansion is modeled using the identity vector $\mathbf{I} = [1, 1, 1, 0, 0, 0]^{\mathrm{T}}$ for three-dimensional problems. The consistent mass matrix $\mathbf{M}_e$, derived from the element's mass distribution, couples with the radial position vector $\mathbf{R}_e$, which is constructed from nodal coordinates projected onto the radial plane perpendicular to the rotation axis. The angular velocity ω governs the magnitude and distribution of centrifugal forces.

Moreover, the expression for the global stiffness matrix $\mathbf{K}$ is given by

$$\mathbf{K} = \sum_{e=1}^{N_e} \mathbf{K}_e = \sum_{e=1}^{N_e} \int_{V_e} \mathbf{B}_e^{\mathrm{T}} \mathbf{D}_e \mathbf{B}_e dV \tag{15}$$

3.2 Numerical implementations

3.2.1 Density filtering

To mitigate checkerboard patterns and achieve well-defined optimized configurations, density filtering is indispensable [36]. This work adopts a weighted decaying density filtering technique [26]. By accounting for potential element volume variances, the filtered density $\bar{x}_i$ is calculated via

$$\bar{x}_i = \Psi_i(\mathbf{x}) = \frac{1}{\sum_{k \in S_i} w_{ik} V_k} \sum_{j \in S_i} w_{ij} V_j x_j \tag{16}$$

with

$$\begin{aligned} S_i &= \left\{ j \middle| \left\| \mathbf{r}_j - \mathbf{r}_i \right\| \le r_{\min} \right\} \\ w_{ij} &= r_{\min} - \left\| \mathbf{r}_j - \mathbf{r}_i \right\| \end{aligned} \tag{17}$$

where $\|\cdot\|$ represents the Euclidean norm of a vector, and $\mathbf{r}_j$ denotes the centroid coordinates of element j. The filter radius $r_{\min}$ is defined as the maximum distance between adjacent element centroids, determined based on geometric considerations to ensure numerical stability.

3.2.2 Material interpolation scheme

The material interpolation scheme plays a pivotal role in establishing a direct relationship between the physical quantities of the problem and continuous design variables. This work employs the RAMP interpolation model to address design-dependent loads, including thermal and centrifugal loads. Under this framework, the interpolation functions for the elastic matrix **D** and mass matrix **M** are mathematically formulated as follows:

$$\begin{aligned} \mathbf{D}_i &= \frac{\overline{x}_i}{1+S_{\mathrm{D}}\left(1-\overline{x}_i\right)}\mathbf{D}^{(0)} \\ \mathbf{M}_i &= \frac{\overline{x}_i}{1+S_{\mathrm{M}}\left(1-\overline{x}_i\right)}\mathbf{M}^{(0)} \end{aligned} \tag{18}$$

Here, the superscript (0) denotes the material properties in the fully solid state. $\overline{x}_i$ represents the filtered density, which quantifies the presence ($\overline{x}_i$ = 1) or absence ($\overline{x}_i$ = 0) of solid material in element *i*. The penalty coefficients S_{D} and S_{M} govern the interpolation of the elastic matrix and mass matrix, respectively.

Additionally, the thermal expansion coefficient α is penalized using the SIMP interpolation model as follows:

$$\alpha_i = \overline{x}_i^{\,p}\alpha^{(0)} \tag{19}$$

where *p* represents the penalty factor of the SIMP interpolation model.

3.2.3 Relaxation strategy of stress-based constraints

In the structural topology optimization under stress-based constraints, the stress singularity phenomenon may sometimes occur. Essentially, this is because the stress becomes discontinuous when the design variables approach zero. To address this "stress singularity phenomenon", the ε-relaxation method can be employed [37]. For the stress calculation of elements with intermediate relative densities, to achieve the relaxation effect, another interpolation scheme similar to the SIMP material interpolation model can be defined as follows:

$$\hat{\boldsymbol{\sigma}}_{ek} = x_e^{p_{\mathrm{m}}}\mathbf{D}^{(0)}\mathbf{B}_{ek}\mathbf{U}_e - x_e^{p_{\mathrm{t}}}\mathbf{D}^{(0)}\alpha^{(0)}\mathbf{I}\Delta T_{ek} \tag{20}$$

Herein, the subscript *ek* denotes the *k*-th integration point of element *e*. For simplification, this study employs the element nodes as integration points. The terms $\hat{\boldsymbol{\sigma}}_{ek}$, $\mathbf{B}_{ek}$, and ΔT_{ek} represent the relaxed stress at the stress integration point, the strain-displacement matrix, and the temperature change respectively. The vector $\mathbf{U}_e$ denotes the displacement vector of element *e*. The parameters p_{m} and p_{t} correspond to the relaxation factors for mechanical and thermal strains, respectively, which take values between zero and one. In this study, relaxation factors are set as $p_{\mathrm{m}} = p_{\mathrm{t}} = 0.5$, following the recommendation in Reference [38].

Thus, under the relaxation strategy of stress-based constraints described above, the mean circumferential stress and mean radial stress in optimization formulation (12) can be further expressed in relaxed form as

$$\begin{aligned}\bar{\sigma}_\theta &= \frac{1}{V_{\text{sum}}}\sum_{e=1}^{n}\left[\frac{1}{o_e}\sum_{k=1}^{o_e}\left(\mathbf{S}_{e,\theta}\hat{\boldsymbol{\sigma}}_{ek}V_e\right)\right]\\ \bar{\sigma}_r &= \frac{1}{V_{\text{sum}}}\sum_{e=1}^{n}\left[\frac{1}{o_e}\sum_{k=1}^{o_e}\left(\mathbf{S}_{e,r}\hat{\boldsymbol{\sigma}}_{ek}V_e\right)\right]\end{aligned} \tag{21}$$

where o_e represents the number of element integration points, which is simplified to the number of element nodes in this study.

4 Sensitivity analysis

To enable efficient gradient-based algorithm implementation for solving optimization problem (12), gradient information of all structural responses with respect to the design variable x_i is required. In density filtering scenarios, sensitivity analysis of any structural response f_{rsp} - whether it be the objective function or a constraint function - with respect to x_i is explicitly derived using the chain rule:

$$\frac{\partial f_{\text{rsp}}}{\partial x_i} = \sum_{j\in S_i}\frac{\partial f_{\text{rsp}}}{\partial \overline{x}_j}\frac{\partial \overline{x}_j}{\partial x_i} = \sum_{j\in S_i}\frac{1}{\sum_{k\in S_j} w_{jk}\left(\mathbf{r}_k\right)V_k}w_{ji}\left(\mathbf{r}_i\right)V_i\frac{\partial f_{\text{rsp}}}{\partial \overline{x}_j} \tag{22}$$

Evidently, during sensitivity calculations for each optimization response, the differentiation approach using the chain rule remains consistent. Consequently, the key differences in sensitivity analysis across various optimization responses primarily lie in the computation of $\partial f_{\text{rsp}} / \partial \overline{x}_i$.

4.1 Sensitivity analysis of the structural compliance

Based on the objective function defined in Equation (12), the expression for the sensitivity of global structural compliance with respect to the filtered density is

$$\frac{\partial C}{\partial \overline{x}_i} = \mathbf{U}^{\mathrm{T}}\mathbf{K}\frac{\partial \mathbf{U}}{\partial \overline{x}_i} + \frac{1}{2}\mathbf{U}^{\mathrm{T}}\frac{\partial \mathbf{K}}{\partial \overline{x}_i}\mathbf{U} \tag{23}$$

Applying the equilibrium equation $\mathbf{KU} = \mathbf{F}^{\mathrm{m}} + \mathbf{F}^{\mathrm{th}} + \mathbf{F}^{\mathrm{ct}}$, the derivative of both sides with respect to $\overline{x}_i$ is taken:

$$\frac{\partial \mathbf{K}}{\partial \overline{x}_i}\mathbf{U} + \mathbf{K}\frac{\partial \mathbf{U}}{\partial \overline{x}_i} = \frac{\partial \mathbf{F}^{\mathrm{m}}}{\partial \overline{x}_i} + \frac{\partial \mathbf{F}^{\mathrm{th}}}{\partial \overline{x}_i} + \frac{\partial \mathbf{F}^{\mathrm{ct}}}{\partial \overline{x}_i} \tag{24}$$

Assuming the mechanical load vector $\mathbf{F}^{\mathrm{m}}$ is independent of the design variables, the derivative $\partial \mathbf{U} / \partial \overline{x}_i$ can be computed by

$$\frac{\partial \mathbf{U}}{\partial \overline{x}_i} = \mathbf{K}^{-1}\left(\frac{\partial \mathbf{F}^{\mathrm{th}}}{\partial \overline{x}_i} + \frac{\partial \mathbf{F}^{\mathrm{ct}}}{\partial \overline{x}_i} - \frac{\partial \mathbf{K}}{\partial \overline{x}_i}\mathbf{U}\right) \tag{25}$$

By substituting Equation (25) into Equation (23), we have the sensitivity of the global compliance written by

$$\frac{\partial C}{\partial \overline{x}_i} = \mathbf{U}_i^{\mathrm{T}}\left(\frac{\partial \mathbf{F}_i^{\mathrm{th}}}{\partial \overline{x}_i} + \frac{\partial \mathbf{F}_i^{\mathrm{ct}}}{\partial \overline{x}_i}\right) - \frac{1}{2}\mathbf{U}_i^{\mathrm{T}}\frac{\partial \mathbf{K}_i}{\partial \overline{x}_i}\mathbf{U}_i \tag{26}$$

Here, respectively, the partial derivatives $\partial \mathbf{F}_i^{\mathrm{th}} / \partial \overline{x}_i$, $\partial \mathbf{F}_i^{\mathrm{ct}} / \partial \overline{x}_i$, and $\partial \mathbf{K}_i / \partial \overline{x}_i$ can be explicitly expressed by Equations (13), (14), and (15) as

$$\begin{aligned}
\frac{\partial \mathbf{F}_i^{\mathrm{th}}}{\partial \overline{x}_i} &= \frac{\overline{x}_i^{\,p}\left[1 + p + S_{\mathrm{D}}\left(1 + p - p\overline{x}_i\right)\right]}{\left[1 + S_{\mathrm{D}}\left(1 - \overline{x}_i\right)\right]^2}\int_{V_i} \mathbf{B}_i^{\mathrm{T}}\mathbf{D}^{(0)}\alpha^{(0)}\mathbf{I}\Delta T_i dV \\
\frac{\partial \mathbf{F}_i^{\mathrm{ct}}}{\partial \overline{x}_i} &= \frac{1 + S_{\mathrm{M}}}{\left[1 + S_{\mathrm{M}}\left(1 - \overline{x}_i\right)\right]^2}\omega^2\mathbf{M}^{(0)}\mathbf{R}_i \\
\frac{\partial \mathbf{K}_i}{\partial \overline{x}_i} &= \frac{1 + S_{\mathrm{D}}}{\left[1 + S_{\mathrm{D}}\left(1 - \overline{x}_i\right)\right]^2}\int_{V_i} \mathbf{B}_i^{\mathrm{T}}\mathbf{D}^{(0)}\mathbf{B}_i dV
\end{aligned} \tag{27}$$

4.2 Sensitivity analysis of mean circumferential/radial stress

Given that the construction forms of mean circumferential stress and mean stress are essentially identical, for brevity, subsequent sensitivity analysis will use the mean circumferential stress as an illustrative example. According to the Equation (21), the sensitivity calculation expression of mean circumferential stress $\overline{\sigma}_\theta$ with respect to the filtered variable $\overline{x}_i$ is:

$$\frac{\partial \overline{\sigma}_\theta}{\partial \overline{x}_i} = \frac{1}{V_{\mathrm{sum}}}\sum_{e=1}^{n}\left[\frac{1}{o_e}\sum_{k=1}^{o_e}\left(\mathbf{S}_{e,\theta}\frac{\partial \hat{\boldsymbol{\sigma}}_{ek}}{\partial \overline{x}_i}V_e\right)\right] \tag{28}$$

Assuming that the temperature difference remains constant within a single iteration, by the chain rule of differentiation and according to Equation (20), the partial derivative of the relaxed mean stress at the *k*-th integration point of element *e* with respect to the design variables can be expressed as:

$$\frac{\partial \hat{\boldsymbol{\sigma}}_{ek}}{\partial \overline{x}_i} = \mathbf{D}^{(0)}\left(\frac{\partial x_e^{p_{\mathrm{m}}}}{\partial \overline{x}_i}\mathbf{B}_{ek}\mathbf{U}_e + x_e^{p_{\mathrm{m}}}\mathbf{B}_{ek}\frac{\partial \mathbf{U}_e}{\partial \overline{x}_i} - \frac{\partial x_e^{p_{\mathrm{t}}}}{\partial \overline{x}_i}\alpha^{(0)}\mathbf{I}\Delta T_{ek}\right) \tag{29}$$

Then, for computational convenience, let

$$\frac{\partial \overline{\sigma}_\theta}{\partial \overline{x}_i} = A_1 + A_2 \tag{30}$$

with

$$A_1 = \frac{1}{V_{\text{sum}}} \sum_{e=1}^{n} \left\{ \frac{1}{o_e} \sum_{k=1}^{o_e} \left[\mathbf{S}_{e,\theta} \mathbf{D}^{(0)} \left(\frac{\partial x_e^{p_\text{m}}}{\partial \overline{x}_i} \mathbf{B}_{ek} \mathbf{U}_e - \frac{\partial x_e^{p_\text{t}}}{\partial \overline{x}_i} \alpha^{(0)} \mathbf{I} \Delta T_{ek} \right) V_e \right] \right\}$$
$$A_2 = \frac{1}{V_{\text{sum}}} \sum_{e=1}^{n} \left\{ \frac{1}{o_e} \sum_{k=1}^{o_e} \left[\mathbf{S}_{e,\theta} \mathbf{D}^{(0)} \left(x_e^{p_\text{m}} \mathbf{B}_{ek} \frac{\partial \mathbf{U}_e}{\partial \overline{x}_i} \right) V_e \right] \right\} \tag{31}$$

For A_1, it can be further simplified to the following expression:

$$A_1 = \frac{1}{V_{\text{sum}} o_i} \sum_{k=1}^{o_i} \left[\mathbf{S}_{i,\theta} \mathbf{D}^{(0)} \left(p_\text{m} x_i^{p_\text{m}-1} \mathbf{B}_{ik} \mathbf{U}_i - p_\text{t} x_i^{p_\text{t}-1} \alpha^{(0)} \mathbf{I} \Delta T_{ik} \right) V_i \right] \tag{32}$$

A_2 can be solved via the adjoint method. First, the element displacement vector $\mathbf{U}_e$ can be obtained from the global displacement matrix $\mathbf{U}$ through the index matrix $\mathbf{\Lambda}_e$, i.e., $\mathbf{U}_e = \mathbf{\Lambda}_e \mathbf{U}$, yielding:

$$\frac{\partial \mathbf{U}_e}{\partial \overline{x}_i} = \mathbf{\Lambda}_e \frac{\partial \mathbf{U}}{\partial \overline{x}_i} = \mathbf{\Lambda}_e \mathbf{K}^{-1} \left(\frac{\partial \mathbf{F}^{\text{th}}}{\partial \overline{x}_i} + \frac{\partial \mathbf{F}^{\text{ct}}}{\partial \overline{x}_i} - \frac{\partial \mathbf{K}}{\partial \overline{x}_i} \mathbf{U} \right) \tag{33}$$

By substituting Equation (33) into A_2, we have

$$\begin{aligned} A_2 &= \frac{1}{V_{\text{sum}}} \sum_{e=1}^{n} \left\{ \frac{1}{o_e} \sum_{k=1}^{o_e} \left[x_e^{p_\text{m}} V_e \mathbf{S}_{e,\theta} \mathbf{D}^{(0)} \mathbf{B}_{ek} \mathbf{\Lambda}_e \mathbf{K}^{-1} \left(\frac{\partial \mathbf{F}^{\text{th}}}{\partial \overline{x}_i} + \frac{\partial \mathbf{F}^{\text{ct}}}{\partial \overline{x}_i} - \frac{\partial \mathbf{K}}{\partial \overline{x}_i} \mathbf{U} \right) \right] \right\} \\ &= \frac{1}{V_{\text{sum}}} \sum_{e=1}^{n} \left[\frac{1}{o_e} \sum_{k=1}^{o_e} \left(x_e^{p_\text{m}} V_e \mathbf{S}_{e,\theta} \mathbf{D}^{(0)} \mathbf{B}_{ek} \mathbf{\Lambda}_e \right) \right] \mathbf{K}^{-1} \left(\frac{\partial \mathbf{F}^{\text{th}}}{\partial \overline{x}_i} + \frac{\partial \mathbf{F}^{\text{ct}}}{\partial \overline{x}_i} - \frac{\partial \mathbf{K}}{\partial \overline{x}_i} \mathbf{U} \right) \end{aligned} \tag{34}$$

Following the adjoint method, we formulate the adjoint vector $\boldsymbol{\lambda}$ as

$$\boldsymbol{\lambda}^{\text{T}} = \frac{1}{V_{\text{sum}}} \sum_{e=1}^{n} \left[\frac{1}{o_e} \sum_{k=1}^{o_e} \left(x_e^{p_\text{m}} V_e \mathbf{S}_{e,\theta} \mathbf{D}^{(0)} \mathbf{B}_{ek} \mathbf{\Lambda}_e \right) \right] \mathbf{K}^{-1} \tag{35}$$

Then, $\boldsymbol{\lambda}$ can be solved via the adjoint equation as

$$\mathbf{K} \boldsymbol{\lambda} = \frac{1}{V_{\text{sum}}} \sum_{e=1}^{n} \left[\frac{1}{o_e} \sum_{k=1}^{o_e} \left(x_e^{p_\text{m}} V_e \mathbf{S}_{e,\theta} \mathbf{D}^{(0)} \mathbf{B}_{ek} \mathbf{\Lambda}_e \right) \right]^{\text{T}} \tag{36}$$

Therefore, the equation A_2 can be simplified to

$$A_2 = \boldsymbol{\lambda}^{\text{T}} \left(\frac{\partial \mathbf{F}^{\text{th}}}{\partial \overline{x}_i} + \frac{\partial \mathbf{F}^{\text{ct}}}{\partial \overline{x}_i} - \frac{\partial \mathbf{K}}{\partial \overline{x}_i} \mathbf{U} \right) \tag{37}$$

where the three partial derivative terms in the right-hand side are calculated via Equation (27). At this stage, the explicit computational expression for the mean circumferential stress sensitivity has been successfully derived.

5 Numerical example

In this section, a numerical example is presented to validate the effectiveness of the proposed topology optimization method incorporating mean circumferential stress constraint. A comparative study compares two configurations: one with mean stress constraints and one without, under identical boundary conditions, aiming to investigate whether this method effectively reduces mean circumferential stress and thereby enhances predicted burst speeds. The gradient-based Global Convergence Method of Moving Asymptotes (GCMMA) algorithm [39] is employed to solve the optimization problem, with convergence criteria defined as: (1) relative variation of the objective function remaining below 0.1% for five consecutive iterations, and (2) full satisfaction of all constraints.

The annular computational model with 100 mm outer diameter, 50 mm inner diameter, and 1 mm uniform thickness features six equally spaced circumferential grooves along its outer periphery as shown in Figure 1. The annular structure sustains a 500 K temperature rise, 7500 rpm rotational velocity, and 989.95 N concentrated mechanical loads at each groove-decomposed into radially outward and clockwise tangential components. Boundary conditions enforce fixed constraints along the innermost circumference while reserving single-layer non-design domains at inner/outer annular regions (excluding groove proximity zones) for manufacturing feasibility. Spatial discretization utilizes 37224 eight-node hexahedral elements (36012 in the design domain) with 75768 nodes, maintaining 1 mm average element size. To achieve cyclic symmetry in the structure, six azimuthally periodic constraints are imposed at the groove orientations, complemented by sectorial symmetry constraints within each 60° periodic segment. The solid structure material exhibits a density of 4450 kg/m^3, Young's modulus of 110 GPa, and Poisson's ratio of 0.3, with thermal expansion characteristics defined by a coefficient of 9.0×10^{-6} K^{-1}.

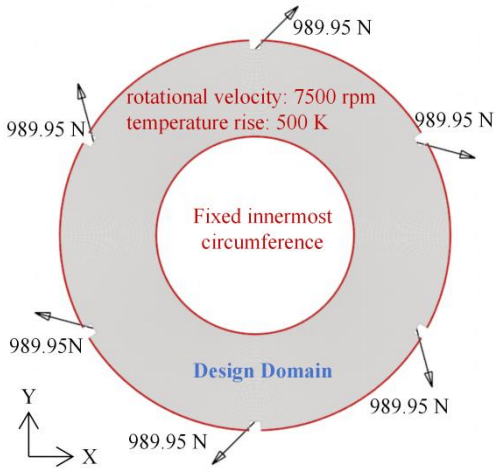

Figure 1: The annular structure with loads and boundary conditions

The initial optimization stage disregards mean circumferential stress constraints, defining the objective function as structural compliance minimization with a volume fraction constraint (upper limit f_V = 0.3). While the mean circumferential stress response is monitored and recorded throughout the optimization process, it remains excluded from the iterative constraint system to establish a baseline reference for subsequent comparative analysis. The optimized structures during the optimization process is illustrated in Figure 2, demonstrating a gradual emergence of hierarchical branching structures with progressive iterations.

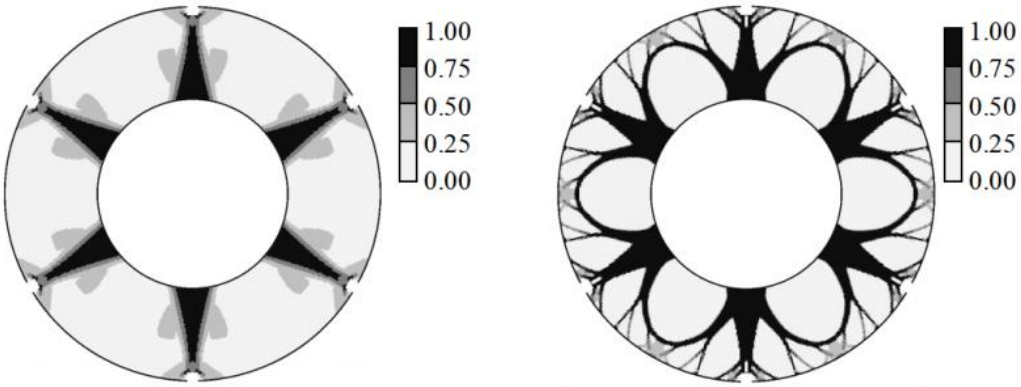

(a) Interation 25 (b) Interation 50

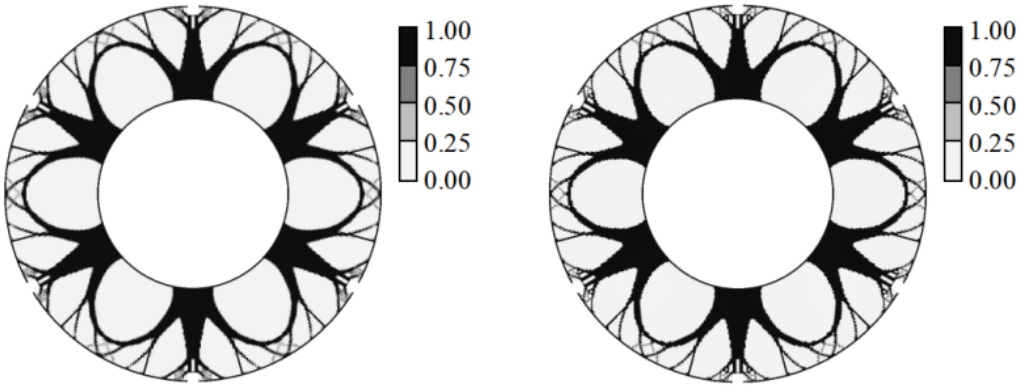

(c) Interation 100 (d) Interation 300

Figure 2: The optimized structures without mean circumferential stress constraint

The iterative response histories encompassing structural compliance, volume fraction, and monitored (unconstrained) mean circumferential stress are demonstrated in Figure 3. The optimization successfully converges with compliance asymptotically approaching 24.39 J and volume fraction consistently tracking the constraint upper bound of 0.3. Notably, the converged mean circumferential stress value of 433.88 MPa serves as a critical reference datum for defining subsequent stress constraint thresholds, providing quantitative guidance for constrained optimization formulations.

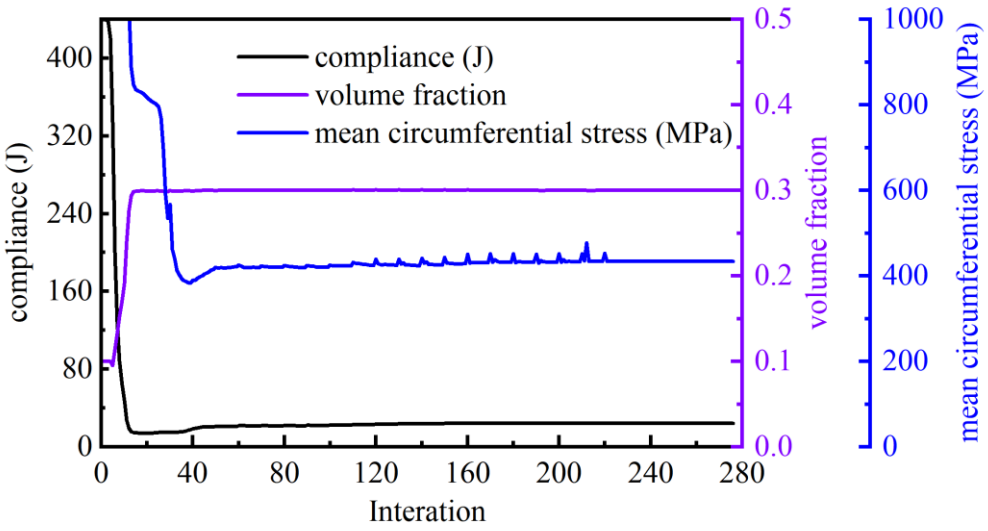

Figure 3: Convergence history of the optimization without mean circumferential stress constraint

Now, we integrate the mean circumferential stress as an optimization constraint into the workflow while maintaining global compliance minimization as the objective and retaining the 0.3 volume fraction constraint. Based on the previous unconstrained optimization's converged stress value of 433.88 MPa, the stress constraint upper bound is set to 400 MPa. Utilizing the unchanged finite element model, Figure 4 demonstrates the evolving optimized structures during iterations. The constrained optimization generates markedly distinct geometries: while preserving the primary trunk-branch motif, additional "sub-trunk structures" emerge between adjacent main trunks, effectively redistributing stress concentrations to satisfy the 400 MPa mean stress threshold. This hierarchical reinforcement pattern demonstrates the constraint's efficacy in balancing global stiffness and localized stress mitigation.

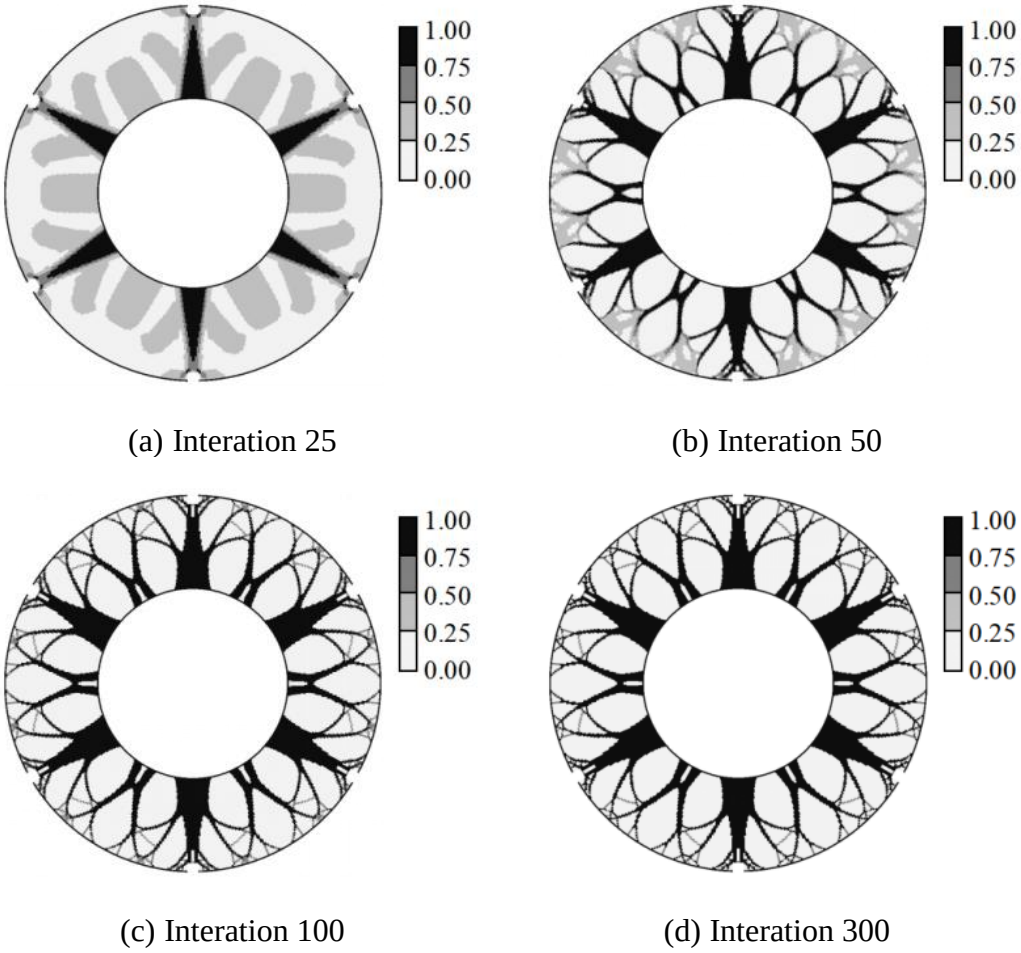

(a) Interation 25 (b) Interation 50

(c) Interation 100 (d) Interation 300

Figure 4: The optimized structures with mean circumferential stress constraint

Figure 5 presents the iterative response histories of all metrics during the optimization process, demonstrating successful convergence with structural compliance asymptotically approaching 23.30 J, volume fraction tracking closely to the 0.3 constraint limit, and mean circumferential stress converging to 395.40 MPa. Notably, the introduction of stress constraints achieves dual performance enhancement: structural stiffness remains uncompromised, while the mean circumferential stress exhibits an 8.87% reduction compared to the baseline configuration, indicating simultaneous improvements in both rigidity and fatigue resistance.

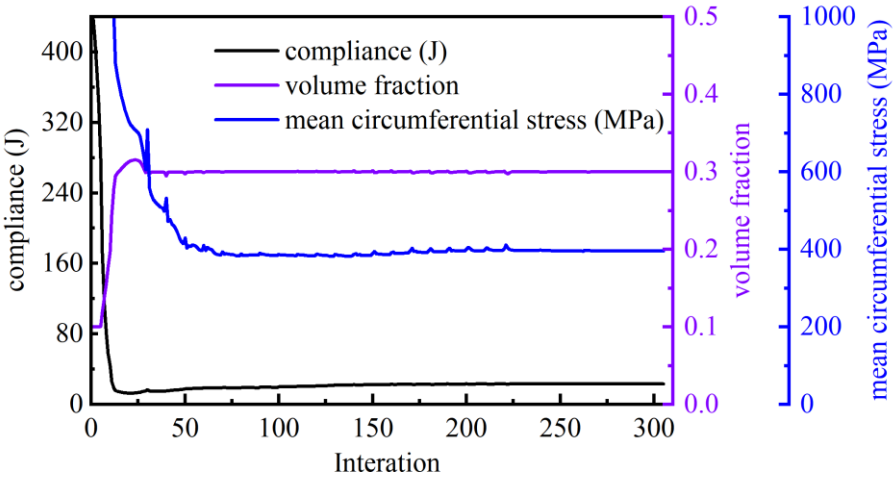

Figure 5: Convergence history of the optimization with mean circumferential stress constraint

Figure 6 comparatively illustrates the evolution profiles of mean circumferential stress with/without constraint implementation during optimization. Both profiles exhibit rapid stress reduction during the initial 50 iterations. Beyond this threshold, the mean stress constraint mechanism activates, coinciding with topological configuration stabilization. From Iteration 50 onward, the constrained case maintains lower stress levels than its unconstrained counterpart, achieving steady-state convergence after Iteration 225. These results validate the efficacy of the proposed mean stress constrained optimization framework in effectively regulating stress distributions while maintaining structural integrity.

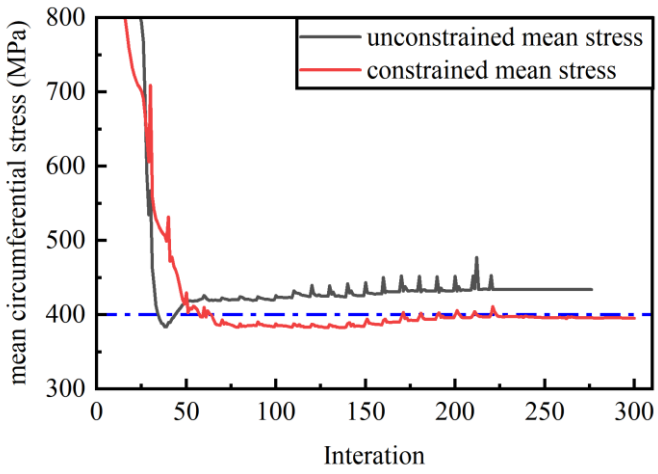

Figure 6: Comparative evolution of mean circumferential stress with and without constraint

6 Conclusions and Contributions

This study introduces a novel topology optimization framework for thermo-elastic cyclic-symmetric structures, integrating mean circumferential/radial stress constraints to enhance burst speed reserve coefficient and structural integrity. By transforming burst speed constraints into equivalent mean stress thresholds, the method balances stiffness maximization with stress regulation, achieving an 8.87% reduction in mean circumferential stress while maintaining structural compliance. Hierarchical branching patterns and sub-trunk structures emerged in optimized designs, demonstrating effective stress redistribution under multi-physics coupling. The framework combines coordinate transformation techniques, adjoint-based sensitivity analysis, and relaxation strategy of stress-based constraints, enabling efficient gradient-based optimization for practical industrial applications.

Key contributions of this study feature threefold: (1) development of a novel mean-stress constrained topology optimization framework for cyclic-symmetric structures, (2) comprehensive validation through an annular structure case study, and (3) establishment of quantitative guidelines for stress threshold determination and stiffness-strength balancing. Future research directions will focus on three extensions: implementation of dynamic load constraints, incorporation of probabilistic failure criteria, and experimental verification through additive manufacturing prototypes to reconcile numerical predictions with physical system behavior.

Acknowledgements

This work is supported by the Defense Industrial Technology Development Program (JCKY2022205B020).

References

[1] Editorial Board of Aero-Engine Design Handbook, "Aero-Engine Design Handbook: Vol. 18, Blade, Disk and Shaft Strength Analysis", Mechanical Industry Press, Beijing, China, 2001.

[2] Department of Defense, "Engine Structural Integrity Program (ENSIP)", United States Air Force, Washington, United States, 2004.

[3] G. Chen, "Aircraft Engine Structural Design and Analysis (2nd ed.)", Beijing Aerospace University Press, Beijing, China, 2014.

[4] S.K. Bhaumik, T.A. Bhaskaran, R. Rangaraju, M.A. Venkataswamy, M.A. Parameswara, R.V. Krishnan, "Failure of Turbine Rotor Blisk of an Aircraft Engine", Engineering Failure Analysis, 9, 287-301, 2002.

[5] E.L. Robinson, "Bursting Tests of Steam-Turbine Disk Wheels", Transactions of the American Society of Mechanical Engineers, 66, 373-380, 1944.

[6] S.B. Macaluso, R.B. Keller, "Liquid rocket engine turbines", NASA, Springfield, US, NASA SP-8110, 1974.

[7] Y.H. Xie, Q. Liu, S.P. Zhu, H.H. Sun, Y. He, Q.Y. Wang, "Burst speed prediction and reliability assessment of turbine disks: Experiments and probabilistic aspects", Engineering Failure Analysis, 145, 107053, 2023.

[8] K. Kasljevic, "Correlation of numerical simulation methods and failure criteria to experimental burst test", Lund University, Lund, Sweden, 2020.
[9] J.C. Zhu, M. Madia, M. Schurig, B. Fedelich, H. Schlums, U. Zerbst, "Burst speed assessment of aero-engine turbine disk based on failure assessment diagram and global stability criterion", Engineering Fracture Mechanics, 277, 2023.
[10] L. Cheng, J.K. Liu, X. Liang, A.C. To, "Coupling lattice structure topology optimization with design-dependent feature evolution for additive manufactured heat conduction design", Computer Methods in Applied Mechanics and Engineering, 332, 408-439, 2018.
[11] L. Meng, W.H. Zhang, D.L. Quan, G.H. Shi, L. Tang, Y.L. Hou, P. Breitkopf, J.H. Zhu, T. Gao, "From Topology Optimization Design to Additive Manufacturing: Today's Success and Tomorrow's Roadmap", Archives of Computational Methods in Engineering, 27(3), 1-26, 2019.
[12] S.C. Sun, T.A. Moreira, B. Rankouhi, X.Y. Yu, I.W. Jentz, D.J. Thoma, M.H. Anderson, X.P. Qian, "Topology optimization, additive manufacturing and thermohydraulic testing of high-temperature heat exchangers". International Journal of Heat and Mass Transfer, 242, 126809-126809, 2025.
[13] M.P. Bendsøe, N. Kikuchi, "Generating Optimal Topologies in Structural Design Using a Homogenization Method", Computer Methods in Applied Mechanics and Engineering, 71, 197-224, 1988.
[14] G.I.N. Rozvany, M. Zhou, T. Birker, "Generalized Shape Optimization without Homogenization", Structural Optimization, 4, 250-252, 1992.
[15] M.P. Bendsøe, O. Sigmund, "Material interpolation schemes in topology optimization", Archive of Applied Mechanics, 69, 635-654, 1999.
[16] T.X. Zuo, H.T. Han, Q.L. Wang, Q.W. Zhao, Z.Y. Liu, "An explicit topology and thickness control approach in SIMP-based topology optimization", Computers and Structures, 307, 107631-107631, 2025.
[17] M. Stolpe, K. Svanberg, "An alternative interpolation scheme for minimum compliance topology optimization", Structural and Multidisciplinary Optimization, 22, 116-124, 2001.
[18] T. Gao, W.H. Zhang, "Topology optimization involving thermo-elastic stress loads", Structural and Multidisciplinary Optimization, 42, 725-738, 2010.
[19] Y.M. Xie, G.P. Steven, "A Simple Evolutionary Procedure for Structural Optimization", Computers & Structures, 49, 885-896, 1993.
[20] O.M. Querin, V. Young, G.P. Steven, Y.M. Xie, "Computational efficiency and validation of bi-directional evolutionary structural optimisation", Computer Methods in Applied Mechanics and Engineering, 189, 559-573, 2000.
[21] M.Y. Wang, X.M. Wang, D.M. Guo, "A level set method for structural topology optimization", Computer Methods in Applied Mechanics and Engineering, 192, 227-246, 2003.
[22] F.H. Scherer, M. Zarroug, H. Naceur, A. Constantinescu, "Topology optimization of curved thick shells using level set method and non-conforming multi-patch isogeometric analysis", Computer Methods in Applied Mechanics and Engineering, 430, 117205-117205, 2024.

[23] Y. Chen, L. Ye, Y.X. Zhang, C.H. Yang, "A multi-material topology optimization with temperature-dependent thermoelastic properties", Engineering Optimization, 54(12), 2140-2155, 2022.
[24] T. Gao, P.L. Xu, W.H. Zhang, "Topology optimization of thermo-elastic structures with multiple materials under mass constraint", Computers & Structures, 173, 150-160, 2016.
[25] G.H. Shi, C.Q. Guan, D.L. Quan, D.T. Wu, L. Tang, T. Gao, "An aerospace bracket designed by thermo-elastic topology optimization and manufactured by additive manufacturing", Chinese Journal of Aeronautics, 33, 1252-1259, 2020.
[26] L. Tang, T. Gao, L.L. Song, C.Q. Zhang, W.H. Zhang, "Thermo-elastic topology optimization of continuum structures subjected to load allocation constraints", Structural and Multidisciplinary Optimization, 65, 2022.
[27] L. Tang, T. Gao, W.T. Zhang, J. Zeng, W.H. Zhang, "Topology optimization of thermo-elastic structures with temperature-dependent material properties under large temperature gradient", International Journal for Numerical Methods in Engineering, 124, 4224-4253, 2023.
[28] L. Alacoque, R.T. Watkins, A.Y. Tamijani, "Stress-based and robust topology optimization for thermoelastic multi-material periodic microstructures", Computer Methods in Applied Mechanics and Engineering, 379, 2021.
[29] Q.X. Meng, B. Xu, C. Wang, L. Zhao, "Stress constrained thermo-elastic topology optimization based on stabilizing control schemes", Journal of Thermal Stresses, 43, 1040-1068, 2020.
[30] B. Wang, G.M. Wang, Y.X. Shi, L. Huang, K. Tian, "Stress-constrained thermo-elastic topology optimization of axisymmetric disks considering temperature-dependent material properties", Mechanics of Advanced Materials and Structures, 29, 7459-7475, 2022.
[31] Q.X. Meng, B. Xu, C.G. Huang, P.J. Han. "Topology optimization of thermo-elastic structures considering stiffness, strength, and temperature constraints over a wide range of temperatures", International Journal for Numerical Methods in Engineering, 123, 1627-1653, 2022.
[32] M. Takalloozadeh, G.H. Yoon, "Development of Pareto topology optimization considering thermal loads", Computer Methods in Applied Mechanics and Engineering, 317, 554-579, 2017.
[33] A.Y. Tamijani, "Stress and stiffness-based topology optimization of two-material thermal structures", Computers & Structures, 256, 2021.
[34] R.F. Silva, P.G. Coelho, F.M. Conde, C.J. Almeida, A.L. Custódio, "Topology optimization of thermo-elastic structures with single and functionally graded materials exploring energy and stress-based formulations", Structural and Multidisciplinary Optimization, 68, 11-11, 2025
[35] Y.L. Feng, Y. He, W, Chen, H.B. Liu, "Analysis and correction of computational methods on disk radial burst speed", Journal of Aerospace Power, 29, 2729-2734, 2014.
[36] O. Sigmund, J. Petersson, "Numerical instabilities in topology optimization: A survey on procedures dealing with checkerboards, mesh-dependencies and local minima", Structural Optimization, 16, 68-75, 1998.

[37] G.D. Cheng, X. Guo, "Epsilon-relaxed approach in structural topology optimization", Structural Optimization, 13, 258-266, 1997.
[38] L. Chau, J. Norato, T. Bruns, C. Ha, D. Tortorelli, "Stress-based topology optimization for continua", Structural and Multidisciplinary Optimization, 41, 605-620, 2010.
[39] K. Svanberg, "A globally convergent version of MMA without line search", in "Proceedings of the First World Congress of Structural and Multidisciplinary Optimization", Goslar, Germany, 9-16, 1995.